



Gas Dynamics of a Luminous $z = 6.13$ Quasar ULAS J1319+0950 Revealed by ALMA High-resolution Observations

Yali Shao^{1,2,3}, Ran Wang², Gareth C. Jones^{3,4}, Chris L. Carilli^{3,5}, Fabian Walter^{3,6,7}, Xiaohui Fan⁸,
Dominik A. Riechers⁹, Frank Bertoldi¹⁰, Jeff Wagg¹¹, Michael A. Strauss¹², Alain Omont¹³, Pierre Cox¹⁴,
Linhua Jiang^{1,2}, Desika Narayanan¹⁵, and Karl M. Menten¹⁶

¹ Department of Astronomy, School of Physics, Peking University, Beijing 100871, China; yshao@nrao.edu

² Kavli Institute for Astronomy and Astrophysics, Peking University, Beijing 100871, China; rwangkaa@pku.edu.cn

³ National Radio Astronomy Observatory, Socorro, NM 87801-0387, USA

⁴ Physics Department, New Mexico Institute of Mining and Technology, Socorro, NM 87801, USA

⁵ Cavendish Laboratory, 19 J. J. Thomson Avenue, Cambridge CB3 0HE, UK

⁶ Max-Planck-Institut für Astronomie, Königstuhl 17, D-69117 Heidelberg, Germany

⁷ Astronomy Department, California Institute of Technology, MC105-24, Pasadena, CA 91125, USA

⁸ Steward Observatory, University of Arizona, 933 North Cherry Avenue, Tucson, AZ 85721, USA

⁹ Department of Astronomy, Cornell University, 220 Space Sciences Building, Ithaca, NY 14853, USA

¹⁰ Argelander-Institut für Astronomie, University at Bonn, Auf dem Hügel 71, D-53121 Bonn, Germany

¹¹ SKA Organization, Lower Withington Macclesfield, Cheshire SK11 9DL, UK

¹² Department of Astrophysical Sciences, Princeton University, Princeton, NJ 08544, USA

¹³ Institut d'Astrophysique de Paris, CNRS and Université Pierre et Marie Curie, Paris, France

¹⁴ Institut de Radioastronomie Millimétrique, St. Martin d'Heres, F-38406, France

¹⁵ Haverford College, 370 W. Lancaster Avenue, Haverford, PA 19041, USA

¹⁶ Max-Planck-Institut für Radioastronomie, Auf dem Hügel 69, D-53121 Bonn, Germany

Received 2017 May 26; revised 2017 July 10; accepted 2017 July 11; published 2017 August 18

Abstract

We present new Atacama Large Millimeter/submillimeter Array (ALMA) observations of the dust continuum and [C II] 158 μm fine structure line emission toward a far-infrared-luminous quasar, ULAS J131911.29+095051.4 at $z = 6.13$, and combine the new Cycle 1 data with ALMA Cycle 0 data. The combined data have an angular resolution of $\sim 0''.3$, and resolve both the dust continuum and the [C II] line emission on a few kiloparsec scales. The [C II] line emission is more irregular than that of the dust continuum emission, which suggests different distributions between the dust and the [C II]-emitting gas. The combined data confirm the [C II] velocity gradient that we had previously detected in a lower-resolution ALMA image from the Cycle 0 data alone. We apply a tilted ring model to the [C II] velocity map to obtain a rotation curve, and constrain the circular velocity to be $427 \pm 55 \text{ km s}^{-1}$ at a radius of 3.2 kpc with an inclination angle of 34° . We measure the dynamical mass within the 3.2 kpc region to be $13.4_{-5.3}^{+7.8} \times 10^{10} M_\odot$. This yields a black-hole and host galaxy mass ratio of $0.020_{-0.007}^{+0.013}$, which is about 4_{-2}^{+3} times higher than that of the present-day $M_{\text{BH}}/M_{\text{bulge}}$ ratio. This suggests that the supermassive black hole grows the bulk of its mass before the formation of most of the stellar mass in this quasar host galaxy in the early universe.

Key words: galaxies: active – galaxies: evolution – galaxies: high-redshift – quasars: general – radio lines: galaxies – submillimeter: galaxies

1. Introduction

In recent years, more than 200 quasars at $5.7 < z < 7.1$ have been discovered in large optical and near-infrared surveys (e.g., Fan et al. 2006; Venemans et al. 2007; Mortlock et al. 2009, 2011; Jiang et al. 2015, 2016; Venemans et al. 2015a; Bañados et al. 2016; Matsuoka et al. 2016; Reed et al. 2017). Millimeter observations of the dust continuum and molecular CO indicate active star formation at rates of a few hundred to a few thousand $M_\odot \text{ yr}^{-1}$ in the host galaxies of about 30% of optically luminous quasars at $z \sim 6$ (e.g., Bertoldi et al. 2003a, 2003b; Petric et al. 2003; Priddey et al. 2003; Wang et al. 2008, 2011). These quasar–starburst systems provide unique laboratories to study the formation of the first supermassive black holes (SMBHs) and their host galaxies close to the end of cosmic reionization.

Bright [C II] 158 μm fine structure line emission has been widely detected in high-redshift quasar–starburst systems (Maiolino et al. 2012; Wang et al. 2013; Willott et al. 2013, 2015; Venemans et al. 2016). The [C II] line is one of the

primary coolants of the star-forming interstellar medium (ISM). Thus, it directly traces the distribution of star formation activity and the kinematic properties of the atomic/ionized gas in quasar host galaxies (Kimball et al. 2015; Díaz-Santos et al. 2016; Venemans et al. 2017). Sixteen quasars at $5.7 < z < 7.1$ are detected in [C II] line emission, with modern submillimeter/millimeter interferometer arrays such as the NOthern Extended Millimeter Array (NOEMA) and Atacama Large Millimeter/submillimeter Array (ALMA; Walter et al. 2009; Venemans et al. 2012, 2016, 2017; Wang et al. 2013, 2016; Willott et al. 2013, 2015; Bañados et al. 2015). These objects have [C II] to far-infrared (FIR) luminosity ratios over a wide range of $(0.19\text{--}4.8) \times 10^{-3}$ (Walter et al. 2009; Willott et al. 2015), indicating that the ISM is in a complex physical state powered by both AGN and star formation activity. The [C II] line emission in 14 of these quasars have been observed with sub-arcsec resolution, and the inferred source sizes are 1.5–3.3 kpc (Walter et al. 2009; Wang et al. 2013; Willott et al. 2013, 2015; Venemans et al. 2016, 2017). Six of the quasars show clear velocity gradients (Wang et al. 2013; Willott et al. 2013),

Table 1
Measured Parameters of J1319+0950

Parameter	Value	
$m_{1450 \text{ \AA}}$ (mag) ^a	19.65	
$S_{1.4 \text{ GHz}}$ (μJy) ^b	64 ± 17	
$S_{250 \text{ GHz}}$ (mJy) ^b	4.20 ± 0.65	
$z_{\text{Mg II}}$ ^a	6.127 ± 0.004	
$z_{\text{CO}(6-5)}$ ^b	6.1321 ± 0.0012	
$\text{FWHM}_{\text{CO}(6-5)}$ (km s^{-1}) ^b	537 ± 123	
	Wang et al. (2013)	This Work
$z_{[\text{C II}]}$	6.1330 ± 0.0007	6.1331 ± 0.0005
$\text{FWHM}_{[\text{C II}]}$ (km s^{-1})	515 ± 81	548 ± 47
$S\Delta\nu_{[\text{C II}]}$ (Jy km s^{-1})	4.34 ± 0.60	4.85 ± 0.40^c 4.31 ± 0.30^d
S_{con} (mJy)	5.23 ± 0.10	4.72 ± 0.17
$\text{Size}_{[\text{C II}]}$ ($''$)	$(0.57 \pm 0.07) \times (0.32 \pm 0.15)$	$(0.62 \pm 0.06) \times (0.51 \pm 0.05)$
$\text{Size}_{[\text{C II}]}$ (kpc)	...	$(3.57 \pm 0.35) \times (2.94 \pm 0.29)$
Size_{con} ($''$)	$(0.39 \pm 0.02) \times (0.34 \pm 0.03)$	$(0.43 \pm 0.02) \times (0.41 \pm 0.02)$
Size_{con} (kpc)	...	$(2.48 \pm 0.12) \times (2.36 \pm 0.12)$

Notes. The source sizes are all in FWHM. The 15% calibration uncertainty is not included in the error bar of the line/continuum flux.

^a Mortlock et al. (2009).

^b Wang et al. (2011).

^c [C II] line flux from the Gaussian fit to the spectral line.

^d [C II] line flux from the 2σ region in the velocity-integrated map.

providing constraints on the dynamical mass. In these objects, the black-hole-to-bulge mass ratio appears to be above the correlation defined by the local objects (Wang et al. 2013). However, these studies were limited by the moderate angular resolution of the early ALMA observations (typically $0''.7$), resulting in a strong degeneracy between the inclination angle and the intrinsic rotational velocity.

In this paper, we report on ALMA Cycle 1 observations of a FIR-luminous quasar ULAS J131911.29+095051.4 (hereafter J1319+0950) at $z = 6.13$, and combine it with ALMA Cycle 0 data to study gas dynamics. Mortlock et al. (2009) discovered this optically bright quasar from the UKIRT Infrared Deep Sky Survey (UKIDSS) with $m_{1450 \text{ \AA}} = 19.65$. Wang et al. (2011) observed this quasar by the Plateau de Bure Interferometer (PdBI) and measured the 250 GHz dust continuum emission using MAMBO, which suggests that it is a very FIR-luminous quasar. They also detected the 1.4 GHz radio continuum and the CO (6–5) line emission. The redshift measured from the CO (6–5) line is consistent with that indicated by the Mg II line. They derived a gas mass of $1.5 \times 10^{10} M_{\odot}$ by adopting the CO excitation model from SDSS J114816.64+525150.3 (Riechers et al. 2009) and a conversion factor of $0.8 M_{\odot} (\text{K km s}^{-1} \text{ pc}^2)^{-1}$. Wang et al. (2013) marginally resolved this quasar in ALMA [C II] observations with a resolution of $0''.7$. Both the line width and the redshift are consistent with those from the CO (6–5) observations. Previous measurements can be seen in Table 1. The [C II] detection reveals a dynamical mass of $12.5 \times 10^{10} M_{\odot}$ with an estimate of the inclination angle (56° , determined from the ratio between the minor and major axis), suggesting an $M_{\text{BH}}/M_{\text{bulge}}$ value that is higher than that of the local value. However, the limit spatial resolution and poor constraint on the inclination angle introduced large uncertainties in the calculation of the gas velocity and host galaxy dynamical mass. This is improved by our new ALMA observations presented here.

The outline of this paper is as follows. In Section 2, we present our ALMA Cycle 1 observations, and combine them

with our ALMA Cycle 0 data (Wang et al. 2013) to measure the dust continuum and [C II] line emission. In Section 3, we discuss the ISM distribution and investigate gas dynamics by applying a tilted ring model to the [C II] velocity map. In Section 4, we summarize our results. Throughout the paper we adopt a Λ CDM cosmology with $H_0 = 71 \text{ km s}^{-1} \text{ Mpc}^{-1}$, $\Omega_M = 0.27$, and $\Omega_{\Lambda} = 0.73$ (Spergel et al. 2007).

2. Observations and Results

2.1. ALMA Observations and Data Reduction

We imaged the [C II] line emission ($\nu_{\text{rest}} = 1900.5369 \text{ GHz}$) of J1319+0950 in 2014 August. We used the ALMA band-6 receivers with thirty-four 12 m antennas in the C34-6 configuration. We tuned one of the 2 GHz spectral windows to the redshifted [C II] line frequency of $\nu_{\text{obs}} = 266.443 \text{ GHz}$ (we adopted the redshift from Wang et al. 2013), and used the other three spectral windows to observe the continuum. The total on-source integration time was 0.6 hr. We calibrated the flux scale based on observations of Titan. The flux calibration uncertainty is $\lesssim 15\%$ for the ALMA Cycle 0 J1319+0950 [C II] observations (Wang et al. 2013), and the typical flux calibration uncertainty is better than 10% for the ALMA Cycle 1 observations (Lundgren 2012). For our combined data, we considered a calibration uncertainty of $\sim 15\%$. The phase was checked by observing a nearby phase calibrator, J1347+1217. The data were reduced using the Common Astronomy Software Application (CASA¹⁷; Version 4.5.0) pipeline. We subtracted the dust continuum under the [C II] line emission in the uv-plane, and binned the data to a channel width of 62.5 MHz ($\sim 70 \text{ km s}^{-1}$) to optimize the data signal-to-noise ratio (S/N) per velocity bin and the sampling of the FWHM of the [C II] spectrum line. We then combined the new data with the ALMA Cycle 0 data (Wang et al. 2013), and made the continuum image and line image data cube from the combined

¹⁷ <https://casa.nrao.edu/>

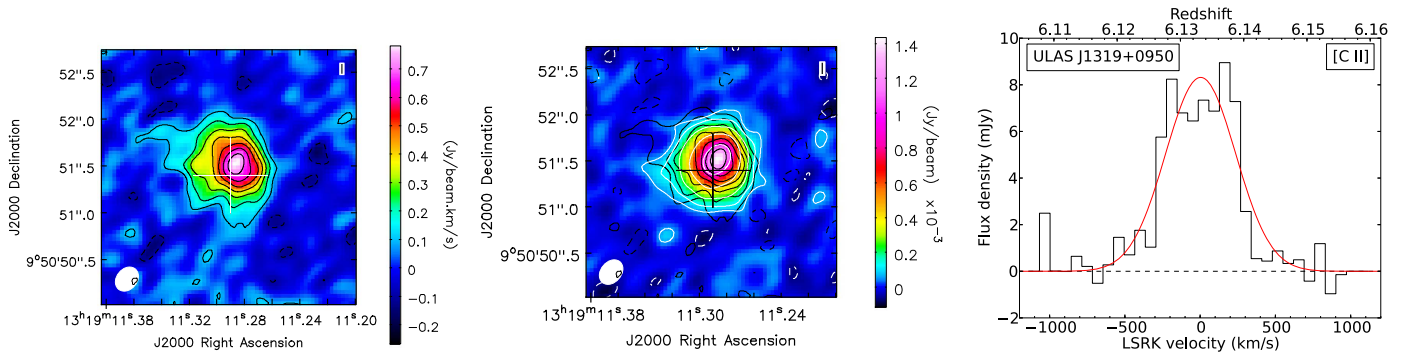


Figure 1. Left: [C II] velocity-integrated map. The white cross is the infrared position presented by Mortlock et al. (2009). The bottom left ellipse shows the size of the restoring beam of $0''.28 \times 0''.22$. The contour levels are $[-2, 2, 4, 6, 8, 10, 12, 14] \times 0.05 \text{ Jy beam}^{-1} \text{ km s}^{-1}$. Center: dust continuum map. The black cross is the infrared position from Mortlock et al. (2009). The bottom left ellipse shows the restoring beam size of $0''.30 \times 0''.22$. The white contours are $[-2, 2, 4, 8, 16, 32] \times 30 \mu\text{Jy beam}^{-1}$. The over-plotted black contours are the same as those in the left panel. Right: [C II] line spectrum (black histogram) over-plotted with the best-fit Gaussian (red line). The LSRK velocity scale is relative to the [C II] redshift from our ALMA Cycle 0 observations (Wang et al. 2013).

data using the CLEAN task in CASA with robust weighting (robust = 0.5). The synthesized beam size of the final [C II] image is $0''.28 \times 0''.22$, corresponding to $1.61 \text{ kpc} \times 1.27 \text{ kpc}$ at the quasar redshift. The 1σ noise is $0.22 \text{ mJy beam}^{-1}$ per 62.5 MHz for the line, and $0.03 \text{ mJy beam}^{-1}$ for the continuum.

2.2. Results

The [C II] line emission and the dust continuum from the combined data are both spatially resolved. We list the observational results in Table 1. The velocity-integrated map of the [C II] line emission is presented in the left panel of Figure 1. We fitted the [C II] line emission with a 2D Gaussian, which yielded a deconvolved source size that is slightly larger than that of the marginally resolved [C II] source size from our ALMA Cycle 0 observations (Wang et al. 2013).

We integrated the intensity from the [C II] line image data cube including the pixels that were determined in the line-emitting region above 2σ in the [C II] velocity-integrated map. The resulting line spectrum is shown as a black histogram in the right panel of Figure 1, with the best-fit Gaussian profile superposed. The Gaussian fit line width is a little larger than, but consistent with, our previous Cycle 0 observations (Wang et al. 2013). The [C II] redshift agrees with the result in Wang et al. (2013). The [C II] line flux calculated from the Gaussian fit is consistent with our previous ALMA observations at a $0''.7$ resolution (Wang et al. 2013) within the calibration uncertainty ($\sim 15\%$). We also got a consistent value by calculating the total flux within the 2σ region in the [C II] intensity map. It is clear that the line profile is flat at the peak in the velocity range from -118 km s^{-1} to 93 km s^{-1} (channel centers). A similar [C II] line profile was also found in a $z = 4.6$ quasar (Kimball et al. 2015). Such a profile suggests that the [C II] line emission originates from a rotating gas disk (see Section 3 for a full analysis).

Figure 2 shows the mean gas velocity map with a clear velocity gradient. It was made using the AIPS¹⁸ XGAUS task with a 2σ flux cut at each position by a Gaussian spectral fit. We also show the [C II] line channel maps in Figure 3. They suggest a clear [C II] line emission shift ($\sim 0''.4$) from 234 to -259 km s^{-1} , which is consistent with the velocity map.

We present the dust continuum map in the center panel of Figure 1. A 2D Gaussian fit shows a source size that is a little

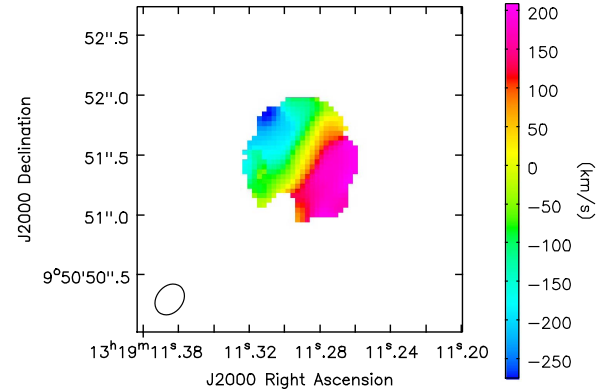


Figure 2. Mean gas velocity map based on the Gaussian fit.

bigger than, but consistent with the result in the Cycle 0 detection (Wang et al. 2013). The total dust continuum emission is comparable to that of the emission detected in the previous $0''.7$ resolution observations (Wang et al. 2013), considering the $\sim 15\%$ calibration uncertainty. We plotted the continuum and [C II] contours (white and black lines) over the dust continuum map. The peak of the dust continuum emission is approximately consistent with that of the [C II] line emission. However, the [C II] line emission looks more irregular than the dust continuum even in high S/N regions (e.g., $>4\sigma$). This may indicate different distributions between the [C II]-emitting gas and the dust component in the central few kiloparsec region.

3. Discussion

3.1. Gas, Dust, and Star Formation Distribution

Wang et al. (2011) presented a gas mass of $1.5 \times 10^{10} M_{\odot}$ by PdBI CO (6–5) observations. Adopting the maximal radius of 3.2 kpc derived in our dynamical fit (Section 3.2) and assuming the same size for the [C II] and CO(2–1) emission, we can derive a gas mass surface density of 466 ($\sim 10^{2.67}$) $M_{\odot} \text{ pc}^{-2}$. This is within the typical range of other star-forming systems at low and high redshifts, e.g., $z = 1$ – 3.5 submillimeter galaxies (SMGs; $10^{2.30}$ – $10^{4.00} M_{\odot} \text{ pc}^{-2}$; Bouché et al. 2007), $z = 1$ – 2.3 BzK-selected galaxies ($10^{1.83}$ – $10^{3.42} M_{\odot} \text{ pc}^{-2}$; Daddi et al. 2010; Tacconi et al. 2010), and $z = 0$ starbursts ($10^{2.25}$ – $10^{4.76} M_{\odot} \text{ pc}^{-2}$; Kennicutt 1998b).

¹⁸ <http://www.aips.nrao.edu/>

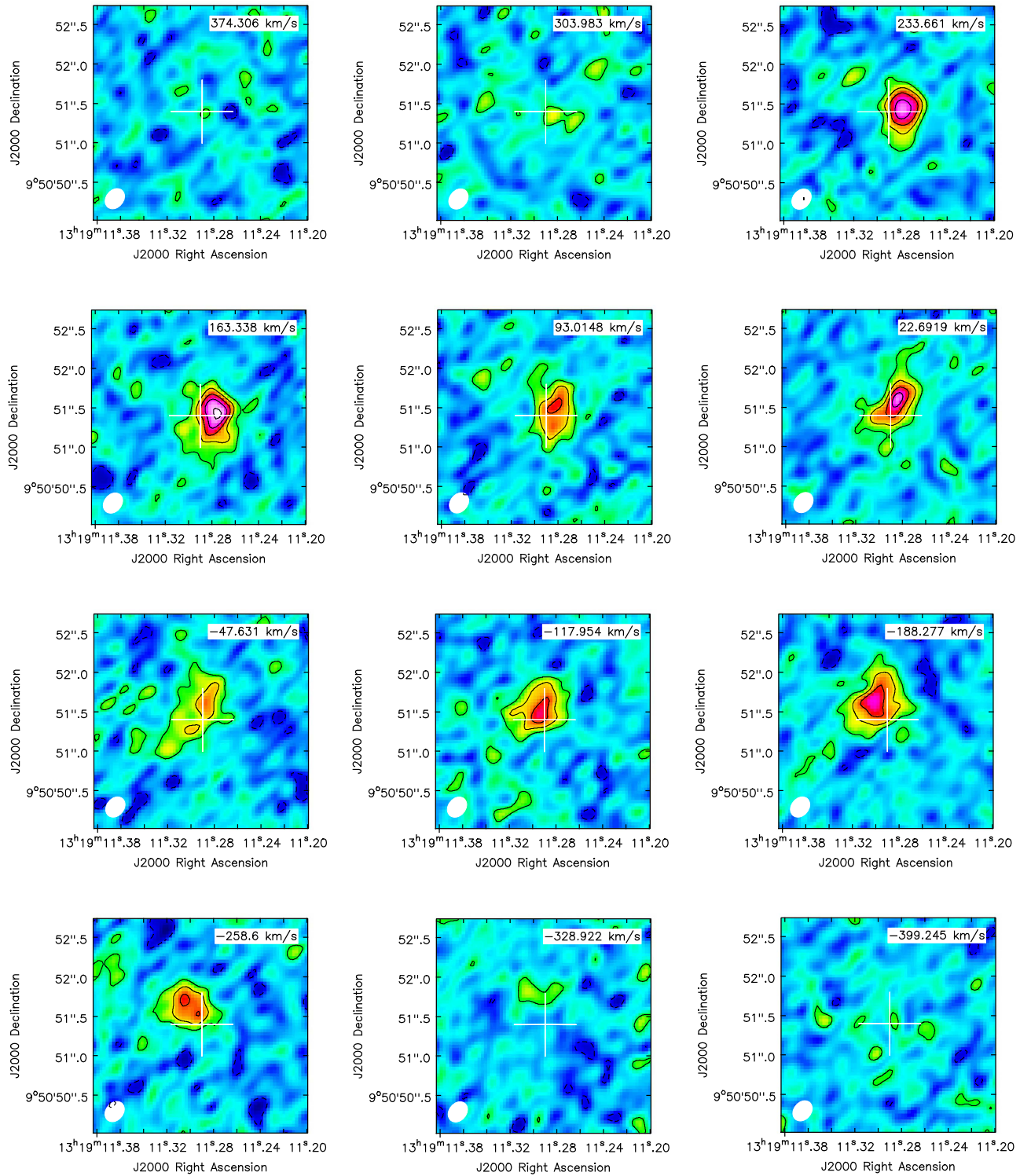


Figure 3. Channel maps of the [C II] line emission in the velocity range from 374 to -399 km s^{-1} . The velocity takes the [C II] redshift from Wang et al. (2013) as a reference. The channel width is $\sim 70 \text{ km s}^{-1}$. The contour levels are $[-2, 2, 4, 6, 8, 10] \times 0.22 \text{ mJy beam}^{-1}$. The white cross represents the UKIRT quasar position (Mortlock et al. 2009). The [C II] line emission is clearly detected in the central eight channels, and the emission peak moves from west to east, shifting about $0''.4$ from 234 to -259 km s^{-1} .

Wang et al. (2013) estimated the FIR luminosity of $(10.7 \pm 1.3) \times 10^{12} L_{\odot}$ by integrating from $42.5 \mu\text{m}$ to $122.5 \mu\text{m}$ in the rest frame and assuming a modified blackbody with a dust temperature of 47 K and an emissivity index of 1.6, which corresponds to an $8\text{--}1000 \mu\text{m}$ luminosity of $(15.0 \pm 1.8) \times 10^{12} L_{\odot}$ (Beelen et al. 2006). However, we

cannot distinguish the FIR emission contributed by the central AGN and star formation activity. We assume a factor of f_{SF} ($0 < f_{\text{SF}} < 1$), which represents the fraction of FIR emission powered by the star formation in the nuclear region. Assuming a Salpeter initial mass function (IMF) and using Equation (4) in Kennicutt (1998a), we can calculate an SFR of

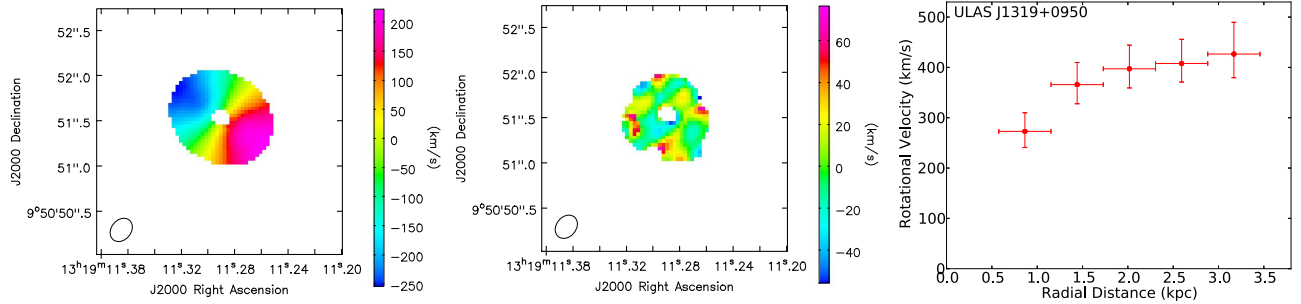


Figure 4. GIPSY modeling result. Panels from left to right: GIPSY modeled velocity map, residual map, and rotation curve. In the left and middle panels, the plotted restored beam size is $0''.28 \times 0''.22$, the same size as the observed [C II] map. There is a hole in the center of the modeled velocity map, because we do not have enough data in the central region to model the dynamical motion.

$(2.6 \pm 0.3) \times f_{\text{SF}} \times 10^3 M_{\odot} \text{ yr}^{-1}$. With the largest gas disk radius of 3.2 kpc proposed in Section 3.2, we calculate an average SFR surface density of $(81 \pm 9) \times f_{\text{SF}} M_{\odot} \text{ yr}^{-1} \text{ kpc}^{-2}$. The values of the SFR and SFR surface density could be lower by a factor of 1.7 if we assume a Chabrier IMF (Chabrier 2003). Our source has a very high SFR surface density that can be comparable to the highest values found in samples of SMGs with a similar gas mass surface density (Bouché et al. 2007; Bothwell et al. 2010; Hodge et al. 2015), if we assume that all the dust continuum is produced by star formation.

3.2. Gas Dynamics in the Quasar Host Galaxy

3.2.1. GIPSY Modeling of Gas Dynamics

Both the flat-peak line profile in the right panel of Figure 1 and the velocity gradient in Figure 2 are consistent with a rotating gas disk. There are also tentative non-rotating structures, e.g., the tail structures in the fifth to seventh channel images in Figure 3. Deeper imaging of these low surface brightness components will determine if there are indeed non-rotating/tidal-like structures in this system and address if there is evidence of a recent galaxy merger.

In our work, we simply assume that the gas has a pure circular rotation in a gas disk and fit the velocity field with a tilted ring model (Rogstad et al. 1974). The tilted ring model decomposes a galaxy into many thin rings, and the dynamic property of each ring at different radii can be described by seven parameters.

1. (x_0, y_0) : the sky coordinates of the rotation center of the galaxy.
2. V_{sys} : the velocity of the center of the galaxy with respect to the Sun.
3. $V_c(R)$: the circular velocity at distance R from the center.
4. $\phi(R)$: the position angle of the major axis on the receding half of the galaxy, taken counterclockwise from the north direction on the sky.
5. $i(R)$: the inclination angle between the normal to the plane of the galaxy and the line-of-sight.
6. $\theta(R)$: the azimuthal angle related to $i(R)$, $\phi(R)$, (x_0, y_0) .

The line-of-sight velocity $V_{\text{los}}(x, y)$ that we observed is a projected value. It is related to the above parameters:

$$V_{\text{los}}(x, y) = V_{\text{sys}} + V_c(R) \sin i \cos \theta \quad (1)$$

$$\cos \theta = \frac{-(x - x_0) \sin \phi + (y - y_0) \cos \phi}{R} \quad (2)$$

$$R^2 = (x - x_0)^2 + (y - y_0)^2. \quad (3)$$

We use the ROTCUR task in the Groningen Image Processing System (GIPSY¹⁹; van der Hulst et al. 1992) to apply the tilted ring model to the observed velocity field to calculate the kinematic parameters. We assume that all of the rings share the same (x_0, y_0) , V_{sys} , ϕ , and i . We solve for $V_c(R)$ in five concentric rings, each with a width of $0''.1$ and a central radius from $0''.15$ to $0''.55$. We determine the initial values of i , ϕ , and (x_0, y_0) based on the 2D Gaussian fit to the [C II] intensity map (left panel of Figure 1), and set the initial value of V_{sys} from the Gaussian fit to the [C II] spectrum (right panel of Figure 1). We solve for the five parameters as follows. Because ϕ and i are correlated, we first simultaneously determine them by fixing the initial values of (x_0, y_0) and V_{sys} . The final values of ϕ and i are calculated as the weighted mean of each $\phi(R)$ and $i(R)$, and the uncertainties are taken as the weighted standard deviations (σ_{sdv}) of the fitting parameters (we take $1/\sigma$ as the weighting). Note that only rings with fitting parameter values above 3σ are considered as a successful fit, and are used in the ϕ and i calculation. In particular, only two rings are successful for i calculation. The successful $i(R)$ solutions of the two rings are $38 \pm 10^\circ$ and $32 \pm 6^\circ$. Since (x_0, y_0) and V_{sys} are coupled, we then determine the two parameters simultaneously by fixing ϕ and i as the values derived from the previous step. We calculate their final values and uncertainties with the same method above. The quoted errors of these parameters are only fitting-type errors, which do not account for the covariance between these parameters. Similar dynamical analysis with ROTCUR can be seen in G. Jones et al. (in preparation).

The final fitting values and weighted standard deviations of V_{sys} , ϕ , and i are $-15 \pm 3 \text{ km s}^{-1}$, $237 \pm 4^\circ$, and $34 \pm 4^\circ$, respectively. There are two other input values to be declared in ROTCUR: free angle and weighting. Following the recommendation by Lucero et al. (2015), we adopt a UNIFORM weighting and an exclusion angle of 0° to use for all of the data with the same weighting.

3.2.2. Rotation Curve

We obtain the rotation curve by adopting the final values of (x_0, y_0) , V_{sys} , ϕ , and i with ROTCUR. We estimate the error bars of the rotational velocities as follows. First we run ROTCUR adopting our standard values of (x_0, y_0) , V_{sys} , and ϕ , but change i by $\pm 1 - \sigma_{\text{sdv}}$. Then we determine the error bars by subtracting these two rotation curves from the one with the best-fit i . In addition, we also add the fitting errors to the final

¹⁹ <https://www.astro.rug.nl/~gipsy/>

errors. We present the rotation curve in the right panel of Figure 4. The curve rises to 2 kpc, and then flattens on larger scales. The circular velocity at the largest radius (i.e., 3.2 kpc) is $42 \pm 55 \text{ km s}^{-1}$. The left panel of Figure 4 shows our modeled velocity field produced by the VELFI task in GIPSY. The residual map is shown in the middle panel with a velocity difference less than 30 km s^{-1} across the entire velocity field.

However, we need to point out that the inclination angle (i) is calculated as the weighted mean of only two successful $i(R)$ values. Thus, the real uncertainty in i could be much larger than that of the error bar mentioned above. There should also exist covariance with other parameters as we cannot fit all the parameters independently at the same time. These will result in large uncertainties in the rotational velocities, which are not included in the error bars shown in Figure 4. A more definite estimate of the error bar of the inclination is undergoing based on the model data analysis (G. Jones & Y. Shao et al. 2017, in preparation). In order to give a more realistic estimate of the uncertainty in the rotational velocity, we check the rotation curve fit with inclination angle values in the range of 26° – 48° , which cover the $i(R)$ values and the 1σ uncertainties that we found with the two successful rings (see Section 3.2.1). The rotational velocity at the largest radius increases to 537 km s^{-1} with $i = 26^\circ$ and decreases to 331 km s^{-1} with $i = 48^\circ$.

In addition, the tilted ring model we adopted in this work does not take into account the effect of the synthesized beam. The beam smearing effect could smooth out any rapid change in the velocity field within the beam (Bosma 1978; Begeman 1987). As was discussed in the extensive studies of the HI-based rotation curves of galaxies, this could affect the inner part of the derived rotation curve, resulting in a shallower slope compared to that of the intrinsic one (Swaters et al. 2000; de Blok & McGaugh 1997) and introduce additional uncertainties in the fitting parameters (e.g., inclination angle, rotation velocity, etc.) of the inner rings (Swaters et al. 2009; Kamphuis et al. 2015). However, the beam smearing effect may not play an important role in our measurements of the outer/flat part of the rotation curve, unless the intrinsic rotation curve is not flat at a large radius (e.g., a solid-body type rotation curve found in dwarf galaxies; de Blok & McGaugh 1997).

3.2.3. $M_{\text{BH}}\text{--}M_{\text{dyn}}$ Relation

Adopting the rotational velocity obtained with the best-fit i of 34° , we calculate the host galaxy dynamical mass within the central 3.2 kpc radius to be $M_{\text{dyn}} = 13.4 \times 10^{10} M_\odot$. The dynamical mass is a little bit higher than that estimated by Wang et al. (2013). Resolving the gas disk with high-resolution imaging is very important to accurately measure the dynamical mass of the distant quasar hosts.

To calculate M_{BH} , we fit the Gemini NIRI spectrum of ULAS J1319+0950 (Mortlock et al. 2009) with a linear continuum, a Gaussian for Mg II line, and an ultraviolet Fe II template based on Shen & Liu (2012; see in Figure 5). We derive a width of the Mg II line to be $34.3 \pm 1.6 \text{ \AA}$ and $L_{3000 \text{ \AA}}$ to be $(3.8 \pm 1.0) \times 10^{46} \text{ erg s}^{-1}$. The final M_{BH} calculated from Equation (3) in Shen & Liu (2012) is $(2.7 \pm 0.6) \times 10^9 M_\odot$. The derived $M_{\text{BH}}/M_{\text{dyn}}$ ratio is 0.020, which is about four times higher than that of the present-day $M_{\text{BH}}/M_{\text{bulge}}$ ratio (0.0051, calculated taking our dynamical mass as the bulge mass by Equation (11) in Kormendy & Ho 2013), suggesting that the SMBH grows its mass earlier than the bulge in this luminous quasar at $z = 6.13$ (Wang et al. 2013).

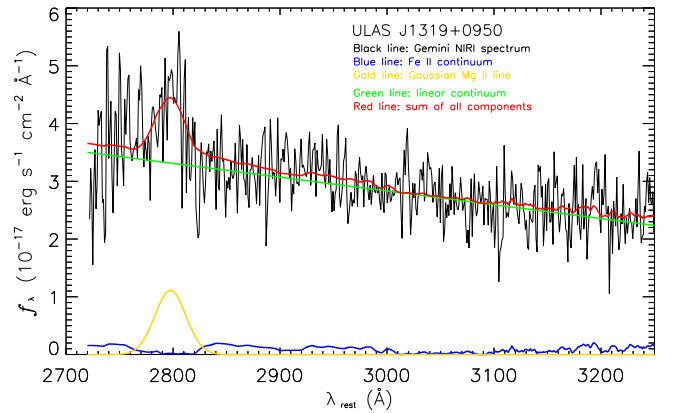


Figure 5. Gemini NIRI spectrum of ULAS J1319+0950 (black line) fitted with a linear continuum (green line), a Gaussian Mg II line (gold line), and an ultraviolet Fe II template (Shen & Liu 2012; blue line). The sum of these components can be seen by the red line.

The dynamical mass would be $21.2 \times 10^{10} M_\odot$ and $8.1 \times 10^{10} M_\odot$ if we adopt the rotational velocities fitted with $i = 26^\circ$ and 48° , respectively. And as a sequence, the $M_{\text{BH}}/M_{\text{dyn}}$ ratio would be 0.013 and 0.033, which are two and seven times higher than those of the local values. Considering these uncertainties, we adopt $M_{\text{dyn}} = 13.4_{-5.3}^{+7.8} \times 10^{10} M_\odot$ and $M_{\text{BH}}/M_{\text{dyn}} = 0.020_{-0.007}^{+0.013}$ as the final measurements of the dynamical mass and mass ratio.

Note that these results are based on a pure rotation disk model. The dynamical property of the gas component in the nuclear region of such a luminous quasar–starburst system could be more complicated, e.g., Curtis & Sijacki (2016) modeled the feedback from a $z \sim 5$ quasar and found a rotational star-forming disk and a strong quasar-driven outflow. With the current data of J1319+0950, we cannot fully rule out that the velocity gradient is due to a bidirectional outflow, which introduces additional uncertainty of the dynamical mass. Deep observations of the [C II]-emitting gas at a higher spatial resolution is required to increase data points for a detailed dynamical model fit, improve the measurement of the disk inclination angle, and address if there is an outflowing gas component in this system.

4. Summary

In this paper, we presented the ALMA Cycle 1 observations of the dust continuum and [C II] line emission in an FIR-luminous quasar J1319+0950 at $z = 6.13$. Combined with our early ALMA Cycle 0 data, we spatially resolved both the dust continuum and the [C II] line emission with an angular resolution of $\sim 0.3''$. The [C II] line emission is more irregular than that of the dust continuum emission, which may suggest a difference in their distributions. The flat-peak feature of the [C II] line spectrum and the clear velocity gradient of the [C II] velocity map indicate that the gas may be in a rotating disk. We used a tilted ring model to fit the [C II] velocity field. Our best-fit results yield an inclination angle of 34° and a circular velocity of $427 \pm 55 \text{ km s}^{-1}$ at a radius of 3.2 kpc. Finally, we calculated an M_{dyn} of $13.4_{-5.3}^{+7.8} \times 10^{10} M_\odot$, and an $M_{\text{BH}}/M_{\text{dyn}}$ ratio of $0.020_{-0.007}^{+0.013}$, which is about 4_{-2}^{+3} times higher than that of the present-day $M_{\text{BH}}/M_{\text{bulge}}$ ratio. This suggests that in this quasar–starburst system, the SMBH evolves earlier than its bulge in the early evolution phase.

This work was supported by the National Key Program for Science and Technology Research and Development (grant 2016YFA0400703) and the China Scholarship Council. G.C.J. is grateful for support from NRAO through the Grote Reber Doctoral Fellowship Program. D.R. acknowledges support from the National Science Foundation under grant number AST-1614213. R.W. acknowledges supports from the National Science Foundation of China (NSFC) grant Nos. 11473004 and 11533001 and the National Key Program for Science and Technology Research and Development (grant 2016YFA0400703). D.N. acknowledges support provided by the National Science Foundation via AST-1724864. We also thank professor D.J. Mortlock for providing the Gemini NIRI spectrum of J1319+0950. This work makes use of the following ALMA data: ADS/JAO.ALMA#2011.0.00206.S and ADS/JAO.ALMA#2012.1.00240.S. ALMA is a partnership of ESO (representing its member states), NSF (USA) and NINS (Japan), together with NRC (Canada), MOST and ASIAA (Taiwan), and KASI (Republic of Korea), in cooperation with the Republic of Chile. The Joint ALMA Observatory is operated by ESO, AUI/NRAO and NAOJ. The National Radio Astronomy Observatory is a facility of the National Science Foundation operated under cooperative agreement by Associated Universities, Inc.

Facility: ALMA.

ORCID iDs

Gareth C. Jones  <https://orcid.org/0000-0002-0267-9024>
 Chris L. Carilli  <https://orcid.org/0000-0001-6647-3861>
 Fabian Walter  <https://orcid.org/0000-0003-4793-7880>
 Xiaohui Fan  <https://orcid.org/0000-0003-3310-0131>
 Dominik A. Riechers  <https://orcid.org/0000-0001-9585-1462>
 Frank Bertoldi  <https://orcid.org/0000-0002-1707-1775>
 Michael A. Strauss  <https://orcid.org/0000-0002-0106-7755>
 Alain Omont  <https://orcid.org/0000-0002-4721-3922>
 Linhua Jiang  <https://orcid.org/0000-0003-4176-6486>
 Desika Narayanan  <https://orcid.org/0000-0002-7064-4309>
 Karl M. Menten  <https://orcid.org/0000-0001-6459-0669>

References

Bañados, E., Decarli, R., Walter, F., et al. 2015, *ApJL*, 805, L8
 Bañados, E., Venemans, B. P., Decarli, R., et al. 2016, *ApJS*, 227, 11
 Beelen, A., Cox, P., Benford, D. J., et al. 2006, *ApJ*, 642, 694
 Begeman, K. G. 1987, PhD Thesis, Kapteyn Institute
 Bertoldi, F., Carilli, C. L., Cox, P., et al. 2003a, *A&A*, 406, L55
 Bertoldi, F., Cox, P., Neri, R., et al. 2003b, *A&A*, 409, L47

Bosma, A. 1978, PhD Thesis, Groningen Univ.
 Bothwell, M. S., Chapman, S. C., Tacconi, L., et al. 2010, *MNRAS*, 405, 219
 Bouché, N., Cresci, G., Davies, R., et al. 2007, *ApJ*, 671, 303
 Chabrier, G. 2003, *ApJL*, 586, L133
 Curtis, M., & Sijacki, D. 2016, *MNRAS*, 457, L34
 Daddi, E., Bournaud, F., Walter, F., et al. 2010, *ApJ*, 713, 686
 de Blok, W. J. G., & McGaugh, S. S. 1997, *MNRAS*, 290, 533
 Díaz-Santos, T., Assef, R. J., Blain, A. W., et al. 2016, *ApJL*, 816, L6
 Fan, X., Carilli, C. L., & Keating, B. 2006, *ARA&A*, 44, 415
 Hodge, J. A., Riechers, D., Decarli, R., et al. 2015, *ApJL*, 798, L18
 Jiang, L., McGreer, I. D., Fan, X., et al. 2015, *AJ*, 149, 188
 Jiang, L., McGreer, I. D., Fan, X., et al. 2016, *ApJ*, 833, 222
 Kamphuis, P., Józsa, G. I. G., Oh, S.-H., et al. 2015, *MNRAS*, 452, 3139
 Kennicutt, R. C., Jr. 1998a, *ARA&A*, 36, 189
 Kennicutt, R. C., Jr. 1998b, *ApJ*, 498, 541
 Kimball, A. E., Lacy, M., Lonsdale, C. J., & Macquart, J.-P. 2015, *MNRAS*, 452, 88
 Kormendy, J., & Ho, L. C. 2013, *ARA&A*, 51, 511
 Lucero, D. M., Carignan, C., Elson, E. C., et al. 2015, *MNRAS*, 450, 3935
 Lundgren, A. 2012, ALMA Cycle 1 Technical Handbook, Version 1.01, <https://almascience.nrao.edu/documents-and-tools/cycle-1/almatechnical-handbook>
 Maiolino, R., Gallerani, S., Neri, R., et al. 2012, *MNRAS*, 425, L66
 Matsuoka, Y., Onoue, M., Kashikawa, N., et al. 2016, *ApJ*, 828, 26
 Mortlock, D., Warren, S., Patel, M., et al. 2011, *Natur*, 474, 616
 Mortlock, D. J., Patel, M., Warren, S. J., et al. 2009, *A&A*, 505, 97
 Petric, A. O., Carilli, C. L., Bertoldi, F., et al. 2003, *AJ*, 126, 15
 Priddey, R. S., Isaak, K. G., McMahon, R. G., Robson, E. I., & Pearson, C. P. 2003, *MNRAS*, 344, L74
 Reed, S. L., McMahon, R. G., Martini, P., et al. 2017, arXiv:1701.04852
 Riechers, D. A., Walter, F., Bertoldi, F., et al. 2009, *ApJ*, 703, 1338
 Rogstad, D. H., Lockhart, I. A., & Wright, M. C. H. 1974, *ApJ*, 193, 309
 Shen, Y., & Liu, X. 2012, *ApJ*, 753, 125
 Spergel, D. N., Bean, R., Doré, O., et al. 2007, *ApJS*, 170, 377
 Swaters, R. A., Madore, B. F., & Trewhella, M. 2000, *ApJL*, 531, L107
 Swaters, R. A., Sancisi, R., van Albada, T. S., & van der Hulst, J. M. 2009, *A&A*, 493, 871
 Tacconi, L. J., Genzel, R., Neri, R., et al. 2010, *Natur*, 463, 781
 van der Hulst, J. M., Terlouw, J. P., Begeman, K. G., Zwitter, W., & Roelfsema, P. R. 1992, in ASP Conf. Ser. 25, Astronomical Data Analysis Software and Systems I, ed. D. M. Worrall, C. Biemesderfer, & J. Barnes (San Francisco, CA: ASP), 131
 Venemans, B. P., Bañados, E., Decarli, R., et al. 2015a, *ApJL*, 801, L11
 Venemans, B. P., McMahon, R. G., Walter, F., et al. 2012, *ApJL*, 751, L25
 Venemans, B. P., McMahon, R. G., Warren, S. J., et al. 2007, *MNRAS*, 376, L76
 Venemans, B. P., Verdoes Kleijn, G. A., Mwebaze, J., et al. 2015b, *MNRAS*, 453, 2259
 Venemans, B. P., Walter, F., Decarli, R., et al. 2017, *ApJ*, 837, 146
 Venemans, B. P., Walter, F., Zschaechner, L., et al. 2016, *ApJ*, 816, 37
 Walter, F., Riechers, D., Cox, P., et al. 2009, *Natur*, 457, 699
 Wang, R., Carilli, C. L., Wagg, J., et al. 2008, *ApJ*, 687, 848
 Wang, R., Wagg, J., Carilli, C. L., et al. 2011, *AJ*, 142, 101
 Wang, R., Wagg, J., Carilli, C. L., et al. 2013, *ApJ*, 773, 44
 Wang, R., Wu, X.-B., Neri, R., et al. 2016, *ApJ*, 830, 53
 Willott, C. J., Bergeron, J., & Omont, A. 2015, *ApJ*, 801, 123
 Willott, C. J., Omont, A., & Bergeron, J. 2013, *ApJ*, 770, 13